J. Fluid Mech. (2008), *vol.* 613, *pp.* 309–327.
doi:10.1017/S0022112008003145 Printed in the United Kingdom

Instability of coupled geostrophic density fronts and its nonlinear evolution

EMILIE SCHERER AND VLADIMIR ZEITLIN

Laboratoire de Météorologie Dynamique, Ecole Normale Supérieure / Université Paris VI,
24 rue Lhomond, 75231 Paris Cedex 5, France
zeitlin@lmd.ens.fr

(Received 19 December 2007 and in revised form 30 June 2008)

Instability of coupled density fronts, and its fully nonlinear evolution are studied within the idealized reduced-gravity rotating shallow-water model. By using the collocation method, we benchmark the classical stability results on zero potential vorticity (PV) fronts and generalize them to non-zero PV fronts. In both cases, we find a series of instability zones intertwined with the stability regions along the along-front wavenumber axis, the most unstable modes being long wave. We then study the nonlinear evolution of the unstable modes with the help of a high-resolution well-balanced finite-volume numerical scheme by initializing it with the unstable modes found from the linear stability analysis. The most unstable long-wave mode evolves as follows: after a couple of inertial periods, the coupled fronts are pinched at some location and a series of weakly connected co-rotating elliptic anticyclonic vortices is formed, thus totally changing the character of the flow. The characteristics of these vortices are close to known rodon lens solutions. The shorter-wave unstable modes from the next instability zones are strongly concentrated in the frontal regions, have sharp gradients, and are saturated owing to dissipation without qualitatively changing the flow pattern.

1. Introduction

Density fronts are ubiquitous in the ocean (Gill 1982). Understanding their dynamics is of obvious importance for comprehension of transport and mixing of mass and momentum. A particular but frequently observed case corresponds to fronts with isopycnals intersecting with the free surface or with the bottom, i.e. outcropping or incropping fronts, respectively. A pair of adjacent outcropping (incropping) fronts with density gradients of opposite sign isolate a fluid of particular density from a surrounding fluid with a different density (Smith 1976; Houghton *et al.* 1982). We focus on outcropping/incropping density fronts in the paper and will call them simply fronts in what follows. Owing to the presence of the Coriolis force, the density fronts should be accompanied by a corresponding velocity jet perpendicular to the density gradients. In the geostrophically balanced (or simply geostrophic) fronts, the Coriolis force and the pressure force are in equilibrium. Such fronts, if they are straight, are exact solutions of the equations of motion (see below). The question of stability of these solutions is of double importance. Besides the stability *per se*, it may be put in the context of the fundamentals in the geophysical fluid dynamics geostrophic adjustment problem (e.g. Reznik, Zeitlin & Ben Jelloul 2001). Namely, starting from

a configuration close to an unstable solution, the question arises as to what will be the end state of the relaxation to the geostrophic equilibrium?

A widely used idealized model for studying dynamics of density fronts is the reduced-gravity rotating shallow-water model, where the effects of density stratification are incorporated in the modified ('reduced') gravity parameter, and the system is modelled by a single-layer finite-depth constant-density fluid. The front corresponds to the fluid terminating at the free streamline (e.g. Killworth 1983*a*), which may be closed (a lens configuration much studied in the literature, Killworth 1983*b*; Cushman-Roisin 1985; Ripa 1987). Coupled density fronts correspond to a band of fluid between two free streamlines (see Griffiths, Killworth & Stern (1982) or more recent references e.g. Rubino, Dotsenko & Brandt 2003). The outcropping/incropping phenomenon is modelled by the fluid terminating at the free streamline with finite slope of the free surface. The model is well-suited for studying the basic dynamics. It obviously neglects the dissipative effects such as Ekman pumping, and oversimplifies stratification. The former may be, in principle, parameterized, for the sake of applications, and the second may be taken into account by using, for example, a two-layer model. In what follows, we will, however, use the simplest version of the model, as in the classical paper by Griffiths *et al.* (1982) which will allow us (i) to complete their stability analysis, and (ii) to understand the nonlinear stage of instability.

The simplest form of the depth profile of the coupled fronts is parabolic. It is easy to see that the corresponding balanced jet has a linear horizontal shear. In what follows, we will focus on this simplest configuration, which may be called the free-streamline rotating shallow-water Couette flow. The classical plane-parallel Couette flow is known to be linearly stable to all infinitesimal perturbations (Drazin & Reid 1981), which is not the case for its (non-rotating) shallow-water counterpart (Knessl & Keller 1995) between the rigid boundaries. In the present case, we have in addition the effects of rotation and free boundaries.

The linear stability of coupled density fronts with parabolic profile within one- and two-layer reduced-gravity models has been studied in the literature, especially in the particular case of zero potential vorticity (PV), which allows for considerable technical simplification. As was shown by Griffiths *et al.* (1982), the coupled fronts with zero-PV are linearly unstable to infinitesimal perturbations with small but finite wavenumbers. Paldor & Ghil (1990) confirmed this result and also found new unstable wavenumber intervals separated by the stability zones for zero-PV fronts; however, they did not display the structure of the new unstable modes. In both papers *ad hoc* zero-PV methods were used for linear stability analysis. Griffiths *et al.* (1982) also gave theoretical arguments for instability of arbitrary (with non-zero PV) coupled density fronts with respect to linearized perturbations with small wavenumbers. In their laboratory experiments, a circular current of buoyant fluid above a deep lower layer was observed to be always unstable, forming a sequence of vortices at the late stages of evolution. It should be noted also that the difference between two-layer and one-layer stability results is mainly the appearance of the short-wave Kelvin–Helmholtz-type instabilities in the former case (Paldor & Ghil 1990), without qualitative changes of the long-wave part of the spectrum which we will be interested in in what follows.

Below, we present a detailed linear stability analysis of the coupled fronts without limiting ourselves by the zero-PV assumption. We use the recent version of the collocation method for linear stability analysis and we benchmark our method by reproducing earlier results on the position of the instability zones and growth rates. We also obtain the detailed structure of the unstable modes for successive instability

zones. After having established the full stability diagram, and confirmed the existence of multiple instability zones with their proper patterns of unstable modes, we perform fully nonlinear high-resolution simulations of the nonlinear stage of instability starting from the coupled fronts perturbed by the unstable mode. We find a specific 'barotropic' breaking, and a complete spatio-temporal reorganization of the flow during the nonlinear evolution of the most unstable long-wave perturbations, while shorter-wave unstable modes from the next instability zones are saturated owing to dissipation without changing the character of the flow.

The paper is organized as follows. After a brief reminder of the rotating shallow-water model and the collocation method in § 2, we present the results of the linear stability analysis in § 3. The nonlinear evolution of the coupled geostrophic fronts perturbed by the unstable modes is presented in § 4. The results are summarized and discussed in § 5. In the Appendix, we briefly present for comparison the results of linear and nonlinear analyses of the frontal configuration with smoothed outcropping, i.e. fluid terminating at the free boundary with zero slope of the free surface.

2. The model and the linear stability problem

2.1. *The model*

The equations of the rotating shallow-water model on the f-plane are:

$$u_t + uu_x + vu_y - fv = -gh_x, \tag{2.1a}$$

$$v_t + uv_x + vv_y + fu = -gh_y, \tag{2.1b}$$

$$h_t + (hu)_x + (hv)_y = 0, \tag{2.1c}$$

where $u(x, y, t)$ is the zonal velocity, $v(x, y, t)$ is the meridional velocity, $h(x, y, t)$ is the fluid depth, f is the Coriolis parameter which we assume to be constant and positive, g is the reduced gravity and the subscripts denote corresponding partial derivatives. We neglect the effects of viscosity and diffusion in the linear stability analysis. The PV is defined as $q = (v_x - u_y + f) / h$. It is a Lagrangian invariant of the model: $\mathrm{d}q/\mathrm{d}t = 0$.

The geostrophic balance corresponds to equilibrium between the Coriolis force and the pressure force in (2.1a) and (2.1b). The straight balanced front, i.e. a geostrophically balanced configuration without dependence on one of the coordinates (say y) is an exact stationary solution of (2.1).

We study stability of a specific geostrophically balanced jet with a parabolic profile:

$$\left.\begin{aligned} h = H &= \begin{cases} \dfrac{H_0}{2}\left(1 - \left(\dfrac{x}{L}\right)^2\right), & |x| \leqslant L, \\ 0, & |x| > L, \end{cases} \\ u &= 0 \\ v = V &= \begin{cases} \dfrac{g}{f} H_x = -\dfrac{gH_0}{fL^2}\, x, & |x| \leqslant L, \\ 0, & |x| > L. \end{cases} \end{aligned}\right\} \tag{2.2}$$

We thus have a free-boundary problem, the bounding streamlines at rest being situated at $x = -L$ and $x = +L$. The fluid terminates with a non-zero slope of the free surface at the boundaries ('drying'), which is a simple, but widely used model of outcroppings/incroppings occurring in the real ocean (see e.g. Griffiths *et al.* 1982;

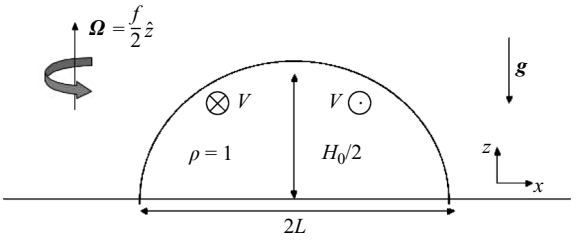

FIGURE 1. The reduced gravity rotating shallow water configuration which models the incropping/outcropping fronts: a layer of fluid of width $L/2$ and maximum depth $H_0/2$ on the rotating plane with Coriolis parameter f and the reduced gravity $\boldsymbol{g}$.

Killworth 1983*a*,*b*; Rubino *et al.* 2003). The basic configuration is schematically presented in figure 1.

The PV of the flow (2.2) is:

$$q = \frac{V_x + f}{H} = \frac{-(gH_0/fL^2) + f}{\frac{1}{2}H_0(1-(x/L)^2)}, \tag{2.3}$$

and vanishes when $V_x = -f$, i.e. $gH_0/fL^2 = f$. Note that in the opposite case, PV is necessarily singular at the free streamlines. This, however, does not pose a problem, unless we use PV as a dynamical variable which is not the case below.

The general criteria of linear stability of the rotating shallow-water flows were established in the classical paper by Ripa (1983): the flow is stable with respect to infinitesimal perturbations if there exists a value of the parameter α such that simultaneously $[V(x)-\alpha]\,\partial_x q(x) \geqslant 0$ and $[V(x)-\alpha]^2 \leqslant gH(x)$ for all x. It is easy to see that Ripa's criteria are not satisfied for the flow (2.2). The first criterion can be written as:

$$\left(-\frac{gH_0}{fL^2} + f\right)\frac{4}{H_0L^2(1-(x/L)^2)^2}\left[-\alpha x - \frac{gH_0}{fL^2}x^2\right] \geqslant 0, \tag{2.4}$$

and can be verified only if $\alpha = 0$ and $gH_0/f^2L^2 \geqslant 1$. The second criterion in the case $\alpha = 0$ becomes:

$$0 \leqslant 1 - \left(\frac{x}{L}\right)^2 - \frac{2\,gH_0}{f^2L^4}\,x^2, \tag{2.5}$$

and is never verified on the interval: $|x| \in]L/(1+2gH_0/(f^2L^2))^{1/2},\ L]$.

We start with a linear stability analysis of the solution (2.2) by benchmarking the results of Griffiths *et al.* (1982) and Paldor & Ghil (1990) which were obtained by the *ad hoc* zero-PV method, and then extend them to the non-zero-PV case, where only the long-wave limit was previously approached (Griffiths *et al.* 1982).

We consider small perturbations of the jet (2.2):

$$h = H + h', \quad u = u', \quad v = V + v', \tag{2.6}$$

and non-dimensionalize the problem with a horizontal length scale L (the half-width of the unpertubed jet), a vertical length scale H_0 (the double of the maximum depth of the unperturbed jet), the inverse of the inertial frequency as the time scale, and the velocity scale fL. The non-dimensionalized equations are:

$$\tilde{u}_{\tilde{t}} + \tilde{u}\tilde{u}_{\tilde{x}} + \tilde{v}\tilde{u}_{\tilde{y}} - \tilde{v} = -Bu\,\tilde{h}_{\tilde{x}}, \tag{2.7a}$$

$$\tilde{v}_{\tilde{t}} + \tilde{u}\tilde{v}_{\tilde{x}} + \tilde{v}\tilde{v}_{\tilde{y}} + \tilde{u} = -Bu\,\tilde{h}_{\tilde{y}}, \tag{2.7b}$$

$$\tilde{h}_{\tilde{t}} + (\tilde{h}\tilde{u})_{\tilde{x}} + (\tilde{h}\tilde{v})_{\tilde{y}} = 0, \tag{2.7c}$$

where $Bu = gH_0/f^2L^2$ is the Burger number, the only non-dimensional parameter governing the problem, and non-dimensional quantities are denoted by a tilde. The background jet is given by:

$$\left.\begin{aligned}\tilde{H}(\tilde{x}) &= \tfrac{1}{2}(1-\tilde{x}^2),\\ \tilde{V}(\tilde{x}) &= -Bu\,\tilde{x}.\end{aligned}\right\} \tag{2.8}$$

Thus, $Bu = 1$ corresponds to the zero-PV jet. We will omit the tildes and the primes in what follows when this does not lead to confusion. Looking for solutions of the non-dimensionalized linearized equations in the form $(u, v, h) = (u_0(x), v_0(x), h_0(x))\,\mathrm{e}^{\mathrm{i}(k\,y-\omega\,t)}$, we obtain:

$$\mathrm{i}\,(k\,V(x)-\omega)\,u_0 - v_0 + Bu\,h_x = 0, \tag{2.9a}$$

$$\mathrm{i}\,(k\,V(x)-\omega)\,v_0 + (1+V(x)_x)\,u_0 + Bu\,\mathrm{i}\,k\,h_0 = 0, \tag{2.9b}$$

$$\mathrm{i}\,(k\,V(x)-\omega)\,h_0 + (u_0\,H(x))_x + \mathrm{i}\,k\,H(x)\,v_0 = 0. \tag{2.9c}$$

This is a free-boundary eigenproblem for eigenvalues ω and eigenvectors (u_0, v_0, h_0). Complex eigenvalues correspond to instabilities.

The boundary conditions are:

$$H(x)+h=0, \qquad \frac{\mathrm{d}L_\pm}{\mathrm{d}t} = u \qquad \text{at } x = L_\pm = \pm 1 + \lambda_\pm, \tag{2.10}$$

where ± 1 are the locations of the free streamlines of the balanced jet and $\lambda_\pm(y,t)$ are the perturbations of the free streamlines. Physically, they correspond to the conditions that the fluid terminates at the boundaries which are the material lines. The linearized boundary conditions give:

(*a*) the relation between the perturbation of the positions of the free streamlines and the value of the height perturbation:

$$\lambda_\pm = -\left.\frac{h_0}{H_x}\right|_{x=\pm 1}, \tag{2.11}$$

(*b*) the continuity equation (2.9*c*) evaluated at $x = \pm 1$.

Hence, the only constraint to impose on the solutions of (2.9) is regularity of (u_0, v_0, h_0) at $x = \pm 1$.

The eigenproblem (2.9) is solved with the help of the collocation method, which has the advantage of allowing us to treat any potential vorticity profile for the basic flow and perturbations with arbitrary wavenumber, whereas in the previous works, Griffiths *et al.* (1982) dealt only with small wavenumbers and Paldor & Ghil (1990) analysed only the zero-PV case. The disadvantage of the method is that it is not specially designed for treating singular eigenproblems. Indeed, the eigenproblem (2.9) has a well-known critical-layer singularity occurring whenever the real part of the eigen phase velocity of the perturbation $c = \omega/k$ is equal to the local flow velocity: $c = V(x)$. Singularities give rise to the stable singular eigenmodes which form a continuous spectrum; see e.g. Vanneste (1998) for a similar albeit simpler geophysical fluid dynamics problem with critical layers. These modes have Dirac-delta or step-function behaviour (depending on the variable) being, in fact distributions, not functions. Discrete counterparts of such singular eigenmodes will be retrieved by the straightforward collocation method. They may be, nevertheless, easily identified by their singular profiles and the fact that they accumulate with increasing resolution (see below). As the non-dimensional velocity of the flow (2.8) takes values between $-Bu$ and $+Bu$, critical levels should appear in the interval $c \in [-Bu, Bu]$. A filtering procedure based on gradient limiters was applied to eliminate these pseudo-modes.

It should be noted that the collocation method was previously applied by Le Sommer, Scherer & Zeitlin (2006) to the problem of stability of the coupled density fronts on the equatorial tangent plane. However, a substantial simplification there was the constant, and not sheared, profile of the background velocity owing to vanishing of the Coriolis force at the equator. Hence, only one critical level appeared and was easy to deal with. The results obtained below demonstrate the efficiency of the collocation method for problems with critical layers.

2.2. *A reminder of the collocation method for the eigenvalue problems*

In order to solve the free-boundary eigenproblem (2.9), we use the pseudospectral collocation method (Trefethen 2000) in the form which was recently applied by Poulin & Flierl (2003) and Le Sommer *et al.* (2006). The system (2.9) on the interval $-1 \leqslant x \leqslant 1$ is discretized on the irregular grid formed by the Chebyshev collocation points, which are unevenly spaced to avoid the Runge phenomenon: $x_j = \cos(j\pi/N), \quad j = 0, 1, \ldots, N$. The Chebyshev differentiation matrix, which will be denoted $\mathscr{D}$, is used as discrete differentiation. The discretized version of the system (2.9) thus follows:

$$\begin{pmatrix} kV & -1 & Bu\,\mathscr{D} \\ (-1 - V_x) & kV & Bu\,k \\ (-H_x - H\mathscr{D}) & kH & kV \end{pmatrix} \begin{pmatrix} u_{00} \\ v_0 \\ h_0 \end{pmatrix} = \omega \begin{pmatrix} u_{00} \\ v_0 \\ h_0 \end{pmatrix}, \tag{2.12}$$

where for convenience we use $u_{00} = \mathrm{i}u_0$. A complete solution of (2.12) with the standard Matlab routine 'eig' is computed in a few seconds on a personal computer.

3. The results of the linear stability analysis

3.1. *Benchmark of the earlier results for flows with zero potential vorticity, $Bu = 1$*

We start with the analysis of the zero-PV case. The real part of the eigen phase-velocities and the imaginary part of the eigenfrequencies (growth rates) as functions of the wavenumber are presented in figure 2. The gradient-limiter filtering is applied in figure 2(*a*) in order to eliminate the pseudo-modes (discrete analogues of singular modes), which fill the band [0, 1] and accumulate with increasing resolution (we present only the positive $c = \mathrm{Re}(\omega)/k$, $\mathrm{Im}\,(\omega)$ part of the graphs, the full ones are obtained by reflection with respect to the abscissa). The typical cross-stream profiles corresponding to a pseudo-mode are presented in figure 3: their main feature is the jump in the along-jet velocity v.

As usual, the instabilities appear when two branches of the dispersion relation for the normal modes intersect, or when the real part of the phase velocity of a mode vanishes (e.g. Hayashi & Young 1987; Sakai 1989). The highest growth rates are found in the small-wavenumber range; however, smaller instability zones exist at higher wavenumbers. We present the cross-stream structure of the most unstable mode in figure 4, and the structure of the associated perturbations of both free streamlines, as calculated from the boundary conditions (2.11), in figure 5. It should be noted that the border streamlines have a significant phase shift, which will be important in the nonlinear evolution of the instability (see below). It is also worth mentioning that, as we checked (not shown), for all instability zones of figure 2, the instability wave pattern is of the type in figure 5, i.e. it is a combination of meandering and varicosity. The structure of the most unstable mode in the second zone of instability is presented in figure 6(*a*). An enlargement of the rightmost instability zone at $k \approx 4.575$ in

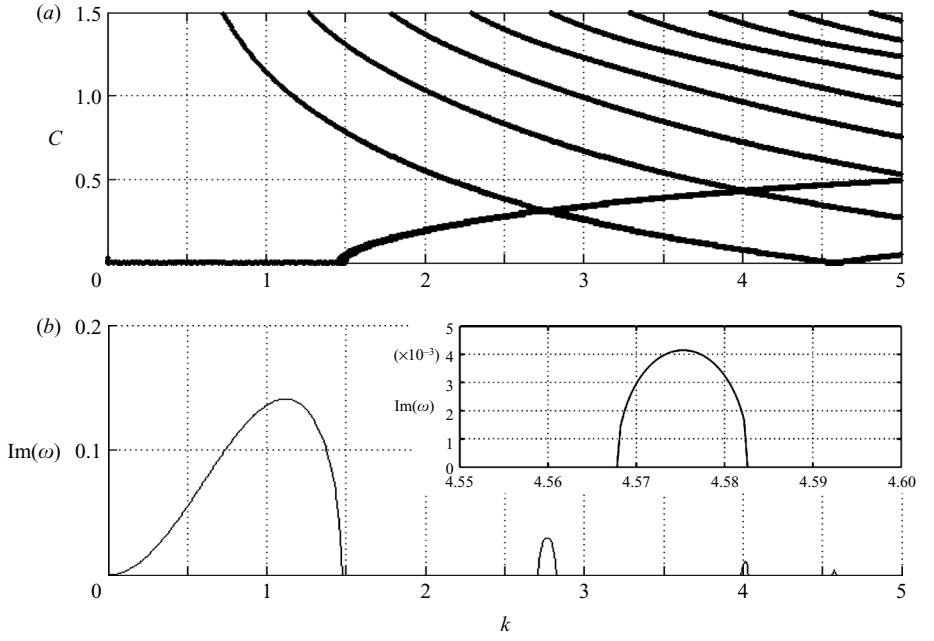

FIGURE 2. (*a*) The eigenvalues of the positive real part of the phase velocity c and (*b*) the growth rate as functions of k for the zero-PV flow $Bu = 1$, $N = 400$. In the $c < 1$ part of (*a*), the eigenvalues corresponding to the pseudo-modes associated with critical levels are filtered out. The instabilities in (*b*) are located where a branch of the phase speed intersects another one, or when the real part of the phase speed vanishes at (*a*). An enlargement of the instability zone at $k \approx 4.575$ is given in the inset.

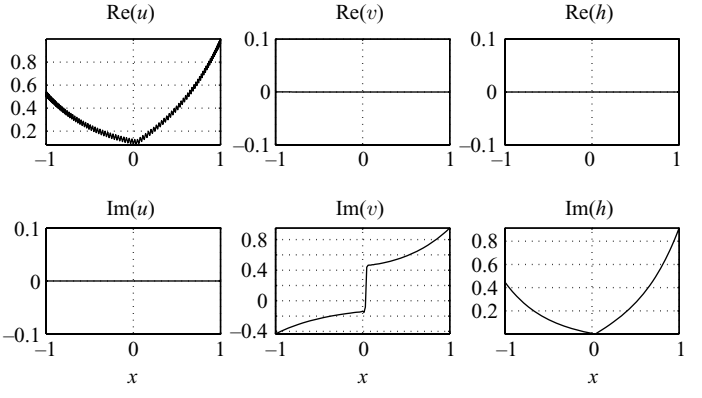

FIGURE 3. Cross-stream structure of the discrete analogue of a singular mode, $k = 1.116$, $\mathrm{Re}(\omega) = 0.043$, $\mathrm{Im}(\omega) = 0$, as captured by the collocation method with $N = 200$.

figure 2 is given in the inset in figure 2 and the structure of the corresponding mode is given in figure 6(*b*). The characteristic features of the higher instability modes are high gradients of the height and velocity fields concentrated in the vicinity of the free streamlines (the unstable modes in the third zone $k \approx 4.01$ have the same structure, not shown).

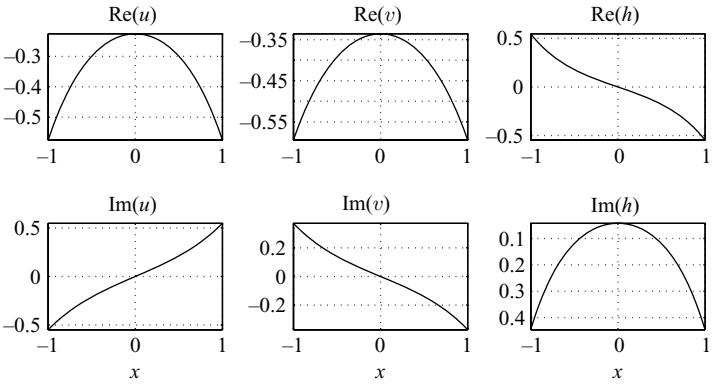

FIGURE 4. Cross-stream structure of the most unstable mode for the zero potential vorticity flow ($Bu = 1$) as calculated by the collocation method $k = 1.116$, $\mathrm{Re}(\omega) = 0$, $\mathrm{Im}(\omega) = 0.14$, $N = 200$.

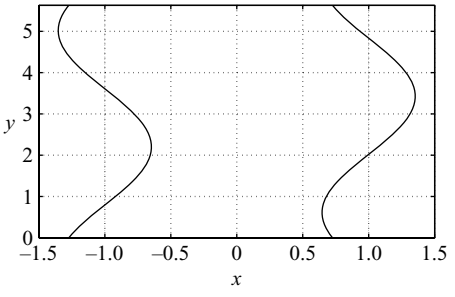

FIGURE 5. The form of the free streamlines of the most unstable mode for the zero-PV flow $Bu = 1$, $k = 1.116$ as derived from the boundary conditions (2.10), (2.11). The steady state corresponds to straight free streamlines at $x = \pm 1$. The amplitude of the deviation from the equilibrium position is purposely exaggerated. The two streamlines have a significant phase shift.

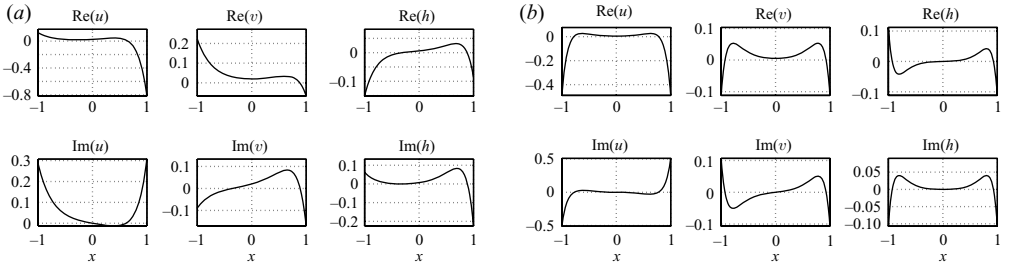

FIGURE 6. (*a*) Cross-stream structure of the most unstable mode in the second zone of instability ($k = 2.77$, $Re(\omega) = 0.89$, $Im(\omega) = 0.03$) for the zero-PV flow ($Bu = 1$) as calculated by the collocation method with $\mathrm{N} = 200$. (*b*) Cross-stream structure of the unstable mode at $k = 4.575$, $\mathrm{Re}(\omega) = 0$, $\mathrm{Im}(\omega) = 0.004$ for the zero-PV flow, $N = 200$.

3.2. *Extension to flows with non-zero potential vorticity, $Bu \neq 1$*

As soon as $Bu \neq 1$, the PV becomes non-zero and non-constant. Griffiths, Killworth & Stern (1982) gave general arguments for the existence of the unstable modes for arbitrary PV. Below we confirm and quantify this prediction. By repeating the

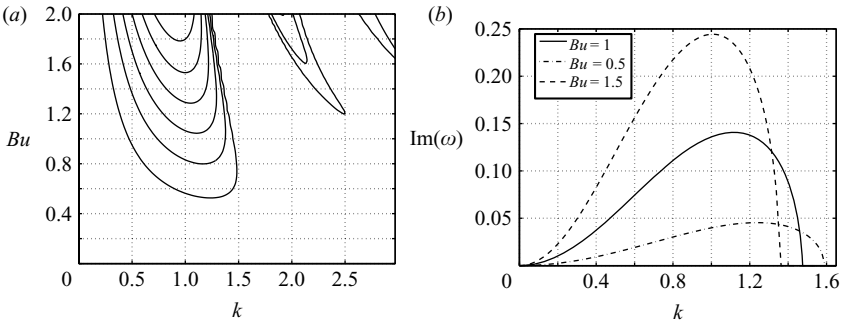

FIGURE 7. (*a*) Stability diagram in the (*Bu, k*)-plane. The isolines of Im(ω) at the values 0.05 up to 0.3 by steps of 0.05 are shown. $N = 200$. (*b*) Growth rates in the main instability zone as functions of the wavenumber for $Bu = 0.5$, $Bu = 1$ (zero-PV flow), and $Bu = 1.5$. For all values of *Bu*, the growth rate at $k = 0$ vanishes. When Bu increases, the maximum growth rate increases and the wavenumber corresponding to the most unstable mode diminishes. 20 collocation points are sufficient to obtain the graph (*b*).

stability analysis for a series of values of the Burger number, we obtained a full stability diagram in the obtained (*Bu, k*)-plane. A part of it corresponding to realistic Burger numbers is presented in figure 7(*a*). Several instability zones are clearly visible. The zone with highest growth rates is the one with lowest wavenumbers. It is the one that was studied in detail by Griffiths *et al.* (1982). Note that when *Bu* increases, the maximum growth rate increases and the wavenumber corresponding to the maximum growth rate diminishes. The growth rates for different values of the Burger number as functions of the wavenumber are shown in figure 7(*b*). The real parts of the phase velocities display a similar behaviour to the case $Bu = 1$ (not shown).

4. Nonlinear evolution of the instability

4.1. *Finite-volume methods for the rotating shallow-water model*

Recent progress in finite-volume numerical schemes for shallow-water equations allows for implementationally simple and quantitatively reliable high-resolution modelling of fully nonlinear dynamics. We use this technique for studying nonlinear evolution of the instabilities of coupled geostrophic density fronts. We apply the high-resolution finite-volume numerical method by Bouchut (2004, 2007) which has the following properties crucial in the present context:

(*a*) it preserves the geostrophic equilibria (i.e. the stationary states in the case of a straight front);

(*b*) it resolves wave breaking and shock formation;

(*c*) it allows us to treat drying.

No explicit dissipation is introduced in the numerical scheme. As was shown in previous applications (Bouchut, Le Sommer & Zeitlin 2004, 2005) energy is extremely well-preserved, the only significant energy loss events being associated with sharp gradient (shock or bore) formation (Bouchut *et al.* 2004), or with reconnection of the streamlines (barotropic Rossby wave breaking, Bouchut *et al.* 2005), which produce localized dissipation zones.

We briefly recall the main ingredients of the method. The shallow-water equations are discretized in the flux-form on a regular grid within the framework of the

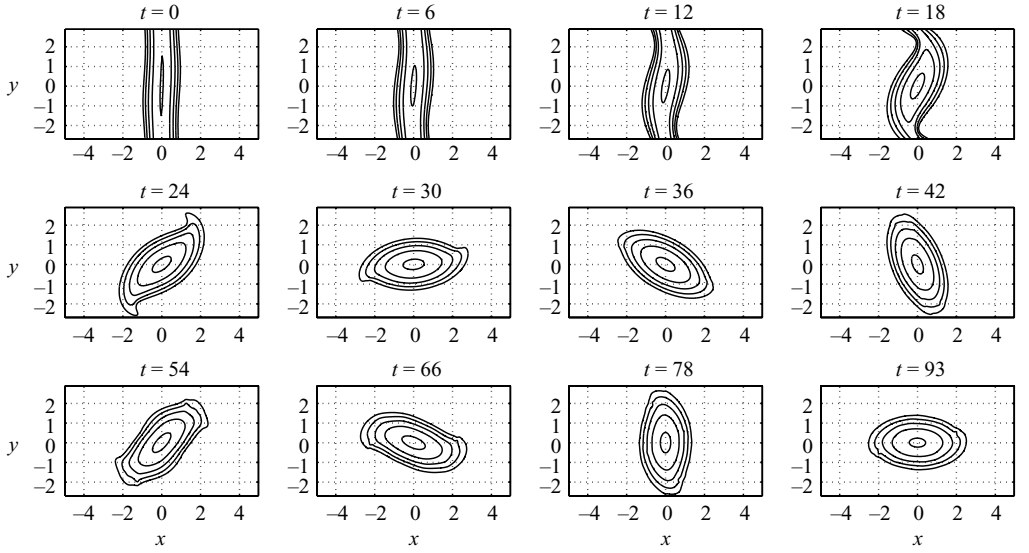

FIGURE 8. Isolines of the fluid depth in the (x, y)-plane: the contours $h = [0.1,\ 0.2,\ 0.3,\ 0.4,\ 0.5]$ are shown. The initial amplitude of the perturbation is 10 % of the maximum depth of the balanced jet. While the instability develops, the jet breaks into a series of anticyclonic rotating lenses/vortices of elliptic shape. The calculation domain is periodic in the y-direction.

finite-volume approach. The finite-volume scheme is then fully prescribed by the choice of the numerical flux function and the treatment of the remaining source terms associated with the Coriolis force. At each time step and in each direction, the Coriolis terms are reformulated following the apparent topography method first introduced by Bouchut *et al.* (2004). The numerical flux function is associated with a relaxation solver adapted to treat topography, as proposed by Audusse *et al.* (2004). This choice of the numerical flux function ensures the ability of the numerical procedure to compute solutions of the shallow-water equations even in the case of terminating depth. The advantage of the scheme is that correct Rankine–Hugoniot conditions guaranteeing the decrease of energy across the shocks are automatically satisfied by the method, i.e. numerical viscosity is indeed a dissipation. The numerical simulations presented hereinafter were obtained with typical resolution 0.05 L and last for a couple of hours on a personal computer.

4.2. *Nonlinear evolution of the most unstable mode*

We simulate the fully nonlinear evolution of the instability corresponding to the most unstable mode, with $k = 1.116$ at $Bu = 1$ (see figure 4). The boundary conditions are periodic in the meridional direction, with period $2\pi/k$ (the results do not change if the period is changed, see below). The numerical method allows for drying, so we compute the solution on the $[-5, 5]$ interval in the zonal direction with sponge boundary conditions. The perturbation of amplitude about 10 % of the maximum height of the unperturbed configuration was superimposed on the background balanced jet. The evolution of the height field in the (x, y)-plane is shown in figure 8. After only a few inertial periods, the instability develops. The jet is pinched, at the same time, the height of the fluid diminishes and becomes very small at pinch locations. A reconnection of the streamlines at this location follows (in other words the unstable boundary waves of figure 5 break), and a series of co-rotating anticyclonic vortices of

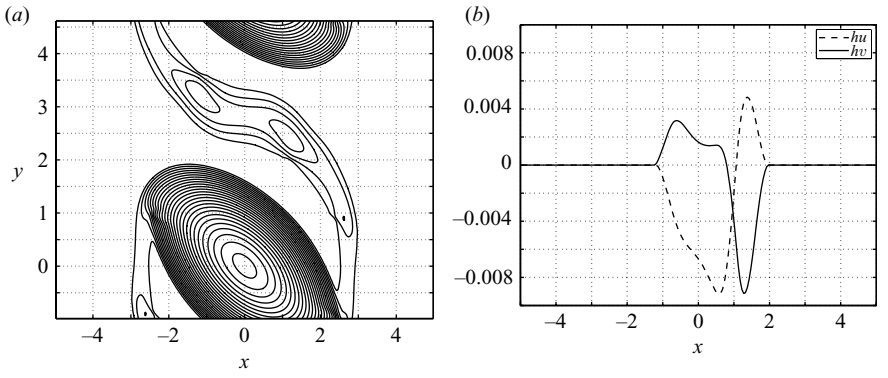

FIGURE 9. (*a*) An enlargement of the isolines of the fluid depth in the (x, y)-plane at $t = 36$ corresponding to the simulation of figure 8: the contours $h = 0.01$ to 0.5 at the interval 0.02 are shown. Filaments of fluid connect the two neighbouring vortices. (*b*) Mass flux along the x-axis across the section $y = 2.5$ at $t = 36$.

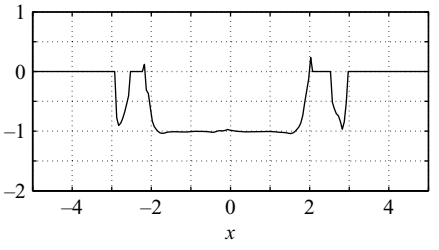

FIGURE 10. Section across $y = 0.1$ of the relative vorticity at $t = 36$, in figure 9. We present the relative vorticity of the regions with $h \geqslant 0.01$. For shallower h, the discretization errors strongly affect the vorticity which is calculated using finite differences.

elliptic shape, weakly connected by the zones carrying a very small amount of fluid, results. A late stage of the evolution is illustrated in figure 9(*a*) where it is seen that the vortices are in fact interconnected by the filaments of fluid of small depth. The mass flux across the filaments at the same moment of time is shown in figure 9(*b*). The amplitude of the mass flux is negligible, and thus the overall flow along initial density fronts is practically disrupted. The vortices hardly interact with each other, apart from the periods of time when they are aligned, with the major axis oriented along the direction of the initial jet. However, even when the major axes are aligned, we observe the values of the mass flux an order of magnitude smaller than in the initial jet, though an order of magnitude greater than the values presented in figure 9(*b*).

A section of the relative vorticity across a vortex is shown in figure 10. The relative vorticity in the vortex core is constant and equal to -1. Outside the core, two zones of negative vorticity are clearly related to the filaments connecting the vortices (see figure 9*a*).

The period of rotation of the vortices is about $T = 60 f^{-1}$. During the whole simulation, one and a third of a full turn is accomplished. The rotating elliptic vortices resemble the rodons, the exact isolated elliptic lens solutions with paraboloidal profile of h (Ripa 1987). We can make a comparison with the period of rotation of a rodon with the same relative vorticity (-1) and the same eccentricity (≈ 2.174). Such a rodon has a period of about $7.6 f^{-1}$ or $36 f^{-1}$ (there exist two families of the rodon

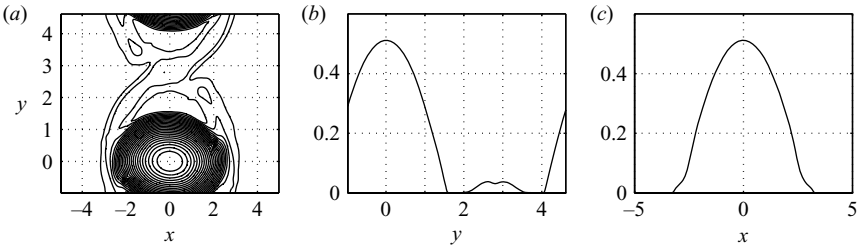

FIGURE 11. (*a*) A snapshot of the fluid depth distribution at $t = 93$, with the same isolines as in figure 9. (*b*) Along-stream section at $x = 0$. (*c*) Across-stream section at $y = 0$. Both cross-sections are accurately fitted by the parabolic profiles for the main vortex part.

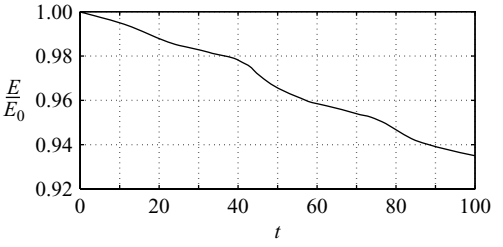

FIGURE 12. Time evolution of the total energy, normalized by the initial total energy for the evolution of the main instability. The events of stronger decrease correspond to the times at which each vortex interacts with its neighbours when their major axes are aligned.

solutions), which gives substantially faster rotation rates. The explanation of the difference is apparently related to the collective and transient character of the vortex structures resulting from our simulation, with rodon-like vortices connected by the rolling up fluid filaments. The detailed structure of the vortex pattern at the late stage of the evolution is presented in figure 11. It is seen that the main vortex is indeed rodon-like with parabolic sections along the main axes, but the amount of fluid in (reconnecting) filaments is still non-negligible.

The time evolution of the total energy of the system is presented in figure 12. Remember that in the numerical scheme we are using, the numerical dissipation acts only in the zones of high gradients (shocks). The slow decrease of energy during the whole simulation is explained by the presence of the drying zones acting as effective shocks, on the one hand, and by the fact that it is easy to generate micro shocks ('shocklets') in the shallow regions of the fluid close to drying. The resulting energy loss is non-negligible during the simulation, but stays sufficiently small (less than 10 %). At times $t = 43$ to 50 and $t = 73$ to 81, events of stronger dissipation take place at times when vortices enter in contact (i.e. when their major axes are aligned). The perturbation created at the periphery of the vortex owing to this interaction, then propagates along the vortex boundary forming shocklets, and dissipates. A snapshot of the spatial distribution of the dissipation rate at the moment of contact between the neighbouring vortices is presented in figure 13(*a*). Dissipation due to shocklets is presented in figure 13(*b*) and shows that the dissipation rate is $\sim 50\,\%$ smaller than the dissipation rate due to reconnection of filaments, but is of the same order of magnitude.

We performed similar experiments with domains of computation of different sizes in the meridional direction, and found that previous results are robust: the most unstable mode from the first instability zone, satisfying the periodicity condition, develops in a similar way.

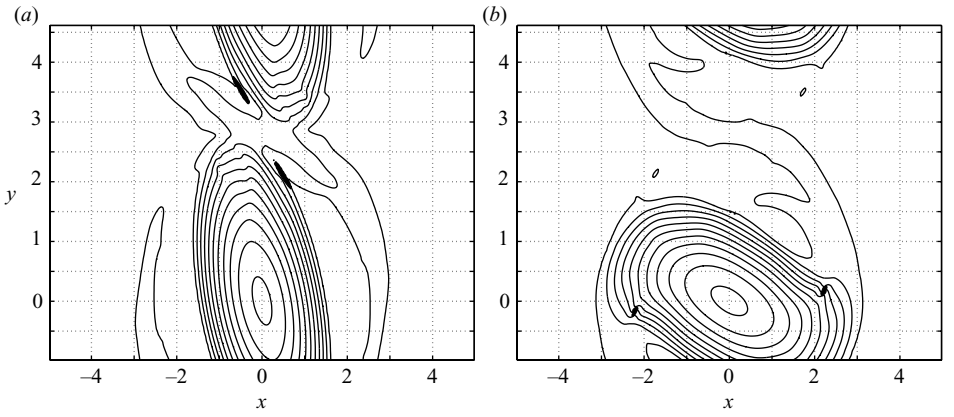

FIGURE 13. Spatial distribution of the dissipation rate superimposed on the isolines of the fluid depth (from h = 0.01 up by step of 0.05). (*a*) At $t = 43$, dissipation is due to reconnections, regions were values of the dissipation rate are between 0.01 and 0.0144 (the maximum value) are shaded. (*b*) At $t = 66$, dissipation is due to shock dissipation, regions where values of the dissipation rate are between 0.004 and 0.0047 (the maximum value) are shaded. Dissipation rate is calculated as the deviation from the energy balance in each cell per time-step, in non-dimensional units.

At $Bu \neq 1$, the process is qualitatively similar. We performed simulations with higher values of the maximum growth rate ($Bu > 1$): the instability develops faster and the rotation rate of the vortices is faster, but there are no significant departures from the described $Bu = 1$ scenario. Simulations with lower values of the maximum growth rate (i.e. with $Bu < 1$) lead to a similar development of the instability as in the $Bu = 1$ case but with a longer time scale and with a slower rotation rate of the vortices.

4.3. *Nonlinear evolution of the modes from the second instability zone*

We then simulated the nonlinear stage of the instability corresponding to higher-wavenumber modes, such as the mode presented in figure 6(*a*). It should be emphasized that this mode, as well as even higher-k unstable modes (see figure 6*b*) has high gradients close to the free streamlines, i.e. at the zones of vanishing depth, and thus is likely to be damped owing to dissipation (as already said the micro shocks, and hence dissipation, are expected in the zone close to the free streamlines). Indeed, we observed a rapid energy decay at the initial stage of the simulation, see figure 15, and had to start with considerable amplitudes of the perturbation (≈ 0.2 to be compared to ≈ 0.1 in the simulations of the most unstable mode above), in order to observe noticeable effects. We present in figure 14 the nonlinear evolution of the mode of figure 6(*a*) superimposed on the balanced flow. The boudary conditions are periodic in the meriodional direction, with period $2\pi/2.77$. We can see a drastic difference with the previous case of the main instability mode. No spatio-temporal reorganization of the mean flow takes place owing to the rapid dissipative saturation of the instability. The asymmetry of the unstable mode with its high gradients at the right-hand boundary leads to almost complete disappearence of the perturbation at the right-hand boundary, whereas at the left-hand boundary it survives at the initial level. The energy loss in the simulations presented in figure 15 is much more rapid than in the case of the main instability mode (see figure 12), happening mainly during the first 10 inertial periods, which explains why the growth is almost immediately arrested.

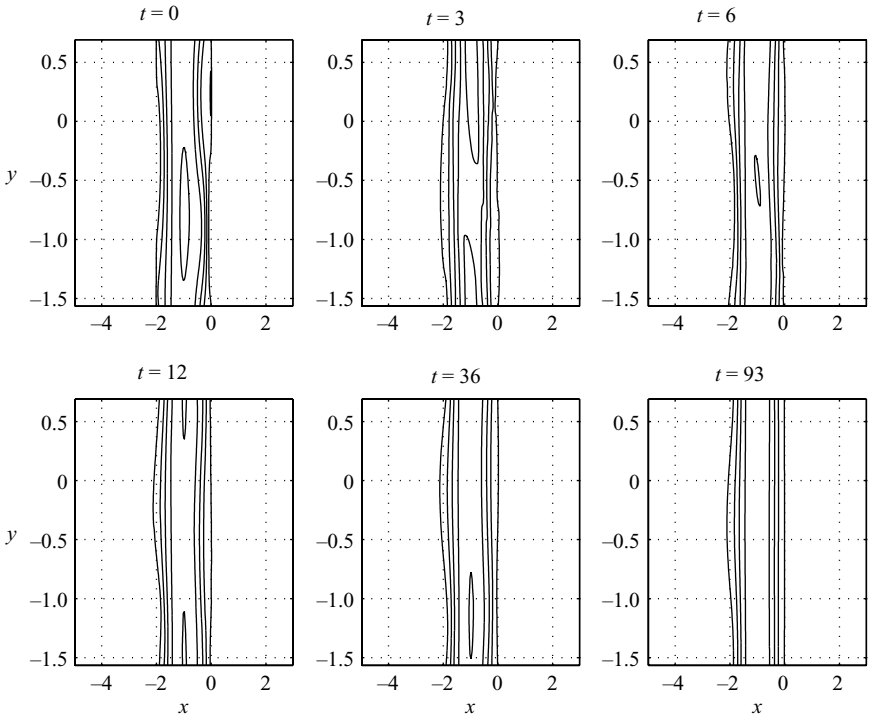

FIGURE 14. Isolines of the fluid depth in the (x, y)-plane for nonlinear evolution of the instability from the second zone: the contours $h = [0.01\ ,\ 0.2\ ,\ 0.3\ ,\ 0.4\ ,\ 0.5]$ are shown. The initial amplitude of the perturbation is 20 % of the maximum depth of the balanced jet. The perturbation is wiped out by dissipation at the right-hand free boundary, where the initial unstable mode had the strongest gradients (see figure 6*a*). The growth is saturated owing to the dissipation at the left-hand boundary, leading to an asymmetric pattern yet close to the initial configuration without significant changes of the mass flux accross the flow, unlike the case of the most unstable mode. The calculation domain is periodic in the y-direction.

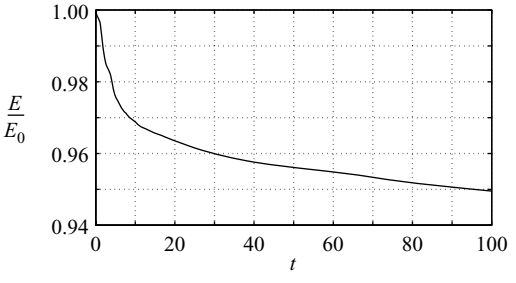

FIGURE 15. Time evolution of the total energy for the instability from the second zone, normalized by the initial total energy. The most significant energy loss takes place at the first 10 inertial periods.

Figure 16 shows the spatial distribution of the dissipation for the initial stages of the evolution of the instability from the second zone. The dissipation is concentrated in the rightmost and leftmost zones of high gradients of the unstable mode with pronounced left–right asymmetry, which explains the eventual disappearence of the perturbation at the right-hand boundary. Note that practically all of the dissipation

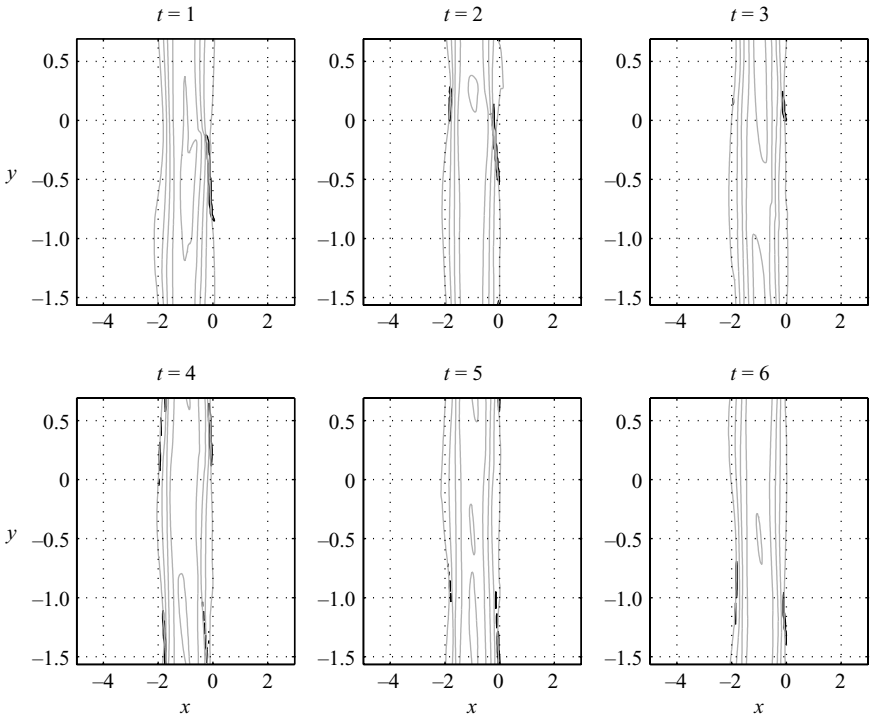

FIGURE 16. Spatial distribution of the dissipation rate (black) superimposed onto the isolines of the fluid depth (grey) for the initial stage of the simulation of figure 14. Zones of the dissipation rate exceeding 6 % of its maximum value are shown.

takes place in the highlighted regions. A similar picture is expected for the unstable modes from the third and fourth instability zones owing to the similar spatial structure of the modes.

Thus, shorter-wavelength modes from the second, third and fourth zones of instability, if excited, are unable to change the structure of the background flow in contradistinction to the main instability mode. This means that in the context of long-time nonlinear evolution of the coupled fronts, the only relevance of these modes is to provide a dissipative sink of energy.

5. Summary and conclusions

We thus revisited the linear stability of the geostrophically balanced coupled density fronts in the reduced-gravity rotating shallow-water model and extended the previously known results to the case of non zero-PV. The flow does not satisfy the stability criteria of Ripa (1983), and we have shown that at any Burger number, it is unstable to perturbations in finite intervals of wavenumbers starting from zero, which are intertwined with stability zones. The wavenumber associated to the maximum growth rate of the instability decreases whereas the Burger number increases, whereas the maximum growth rate itself increases. The detailed structure of the unstable modes, important for understanding their nonlinear evolution, was established. At the same time we demonstrated the capability of the collocation method to efficiently treat complicated configurations with a continuum of critical levels.

The nonlinear evolution of the unstable modes was then investigated with the help of high-resolution numerical simulations, allowing us to resolve the fine-structure details of the dynamics. The main instability was shown to develop by pinching the fronts and forming a row of clockwise rotating elliptic vortices with a parabolic form of the interface similar to the (isolated) exact rodon solutions. The vortices are interacting weakly through the fluid filaments connecting them. Their interaction is more pronounced when the major axes of the vortices are aligned in the direction of the initial jet, leading to enhanced dissipation in the inter-vortex regions. The energy continues to decrease slowly even after a hundred inertial periods meaning that the relaxation towards the (still unknown) adjusted state is very slow. It should be noted that formation of a sequence of elliptic vortices during nonlinear evolution of a zero-PV circular jet was reported in the experiments of Griffiths *et al.* (1982). Yet, the high-resolution numerical simulations allow us to add quantitative and qualitative details, such as measures of fluxes, vorticity, or position of the enhanced mixing zones.

The second-zone instabilities were shown to be subject to the dissipative damping at the initial stages of the evolution owing to the specific spatial structure of the corresponding modes with high gradients concentrated in the outcropping regions. They cannot therefore reorganize the flow, unlike the main unstable mode.

We also provide evidence (see the Appendix), that although the structure of the main unstable mode is sensible to the profile of the mean shear flow, the growth rates and position of the main instability zone on the wavenumber axis, as well as nonlinear evolution of the instability are not. This result is consistent with the general analysis of Griffiths *et al.* (1982).

Finally, it should be mentioned that linear stability results for zero-PV configurations in the two-layer rotating shallow-water model were obtained by Paldor & Ghil (1990). In the most realistic, in the oceanic context, case of a thick upper (lower) layer for outcropping (incropping) fronts the instability zones and growth rates are close to the one-layer ones discussed above. Significant differences appear, however, at relatively thin second layers with the appearance of short-wave instabilities having growth rates higher than the 'main' long-wave instability. They are presumably Kelvin–Helmholtz (KH) like, and their presence may considerably change the nonlinear evolution scenario. It should be stressed that although it is relatively easy to analyse linear stability by the collocation method in this case, the nonlinear simulations in the presence of KH-like instabilities do pose a problem because, as is well known, the two-layer shallow-water equations change type (hyperbolic to elliptic, see e.g. Zeitlin 2007). We plan to give a thorough analysis of the two-layer case elsewhere.

Appendix. A resumé of the linear and nonlinear analysis of coupled fronts with smoothed outcropping

Following a suggestion of an anonymous referee, we present below a brief account of linear and nonlinear analysis of a configuration where the free boundaries are approached at zero slope of the free surface, to be compared with finite-slope outcropping fronts. The height and velocity profiles in non-dimensional terms are chosen as follows in the interval $(-1, 1)$:

$$\left.\begin{aligned} \tilde{H}(\tilde{x}) &= \tfrac{1}{2}\,(1+\cos\pi\tilde{x}), \\ \tilde{V}(\tilde{x}) &= -Bu(\pi/2)\,\sin\pi\tilde{x}, \end{aligned}\right\} \tag{A 1}$$

and are both zero outside this interval.

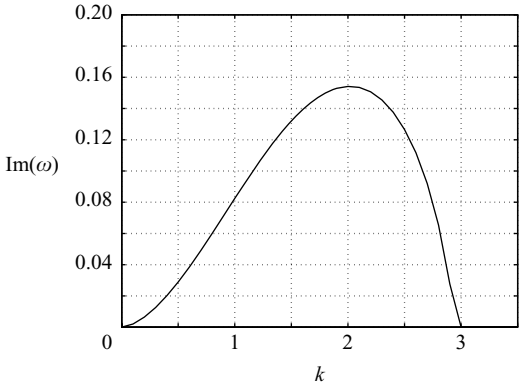

FIGURE 17. The main instability zone for the configuration (A 1) as obtained by the collocation method. $\mathrm{Re}(\omega) = 0$ throughout the zone.

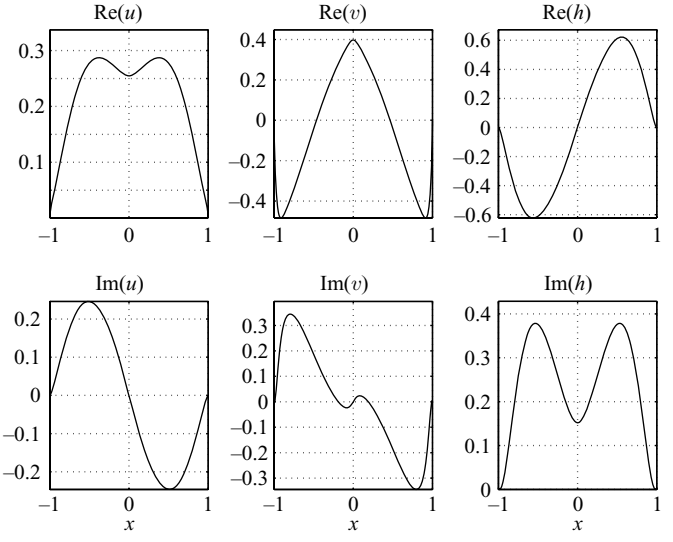

FIGURE 18. The structure of the most unstable mode for the configuration (A 1) with zero-PV as obtained by the collocation method.

As is easy to see, this profile is not stable according to Ripa's criterion. The linear stability analysis of this configuration by the collocation method along the lines of the main text above gives the instability diagram for the most unstable modes presented in figure 17. The typical shear was purposely taken to be the same as for the parabolic flow at zero-PV, which corresponds to $Bu = 2/\pi$ in (A 1). Although the quantitative details are somewhat different, the resemblence with the main instability zone for the parabolic jet is striking. The structure of the most unstable mode presented in figure 18 is, unsurprisingly, different from that for the parabolic profile. It has a more complicated structure with multiple extrema which complicates the filtering of the pseudo-modes. However, if this mode is superimposed onto the basic flow (A 1), the resulting nonlinear evolution displayed in figure 19 is qualitatively and quantitatively close to that presented in figure 8. This indicates that nonlinear evolution of the main instability with its typical reorganization of the flow into a system of co-rotating

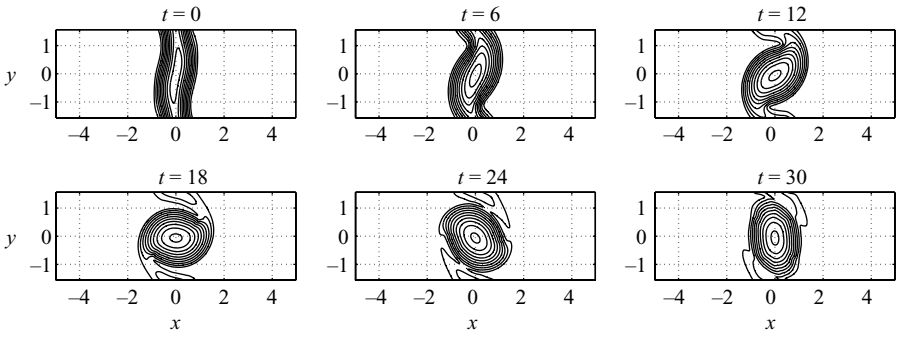

FIGURE 19. The nonlinear evolution of the configuration (A 1) with zero-PV perturbed by the mode of figure 18.

elliptic vortices is robust and not sensitive to the details of the mean flow profile, provided the typical shear is the same.

REFERENCES

AUDUSSE, E., BOUCHUT, F., BRISTEAU, M.-O., KLEIN, R. & PERTHAME, B. 2004 A fast and stable well-balanced scheme with hydrostatic reconstruction for shallow water flows. *SIAM J. Sci. Comput.* **25**, 2050–2065.

BOUCHUT, F. 2004 *Nonlinear Stability of Finite Volume Methods for Hyperbolic Conservation Laws, and Well-Balanced Schemes for Sources*. Birkhauser.

BOUCHUT, F. 2007 Efficient numerical finite-volume schemes for shallow water models. In *Nonlinear Dynamics of Rotating Shallow Water: Methods and Advances* (ed. V. Zeitlin), Elsevier, pp. 191–258.

BOUCHUT, F., LE SOMMER, J. & ZEITLIN, V. 2004 Frontal geostrophic adjustment and non-linear-wave phenomena in one dimensional rotating shallow water. Part 2. High resolution numerical simulations. *J. Fluid Mech.* **514**, 35–63.

BOUCHUT, F., LE SOMMER, J. & ZEITLIN, V. 2005 Breaking of balanced and unbalanced equatorial waves. *Chaos* **15**, 13 503–13 521.

CUSHMAN-ROISIN, B. 1985 Linear stability of large, elliptical warm-core rings. *J. Phys. Oceanogr.* **16**, 1158–1164.

DRAZIN, P. G. & REID, W. H. 1981 *Hydrodynamic Stability*. Cambridge University Press.

GILL, A. E. 1982 *Atmosphere–Ocean Dynamics*. Academic.

GRIFFITHS, R. W., KILLWORTH, P. D. & STERN, M. E. 1982 Ageostrophic instability of ocean currents. *J. Fluid Mech.* **117**, 343–377.

HAYASHI, Y.-Y. & YOUNG, W. R. 1987 Stable and unstable shear modes of rotating parallel flow in shallow water. *J. Fluid Mech.* **184**, 477–504.

HOUGHTON, R. W., SCHLITZ, R., BEARDSLEY, R. C., BUTMAN, B. & CHAMBERLIN, J. L. 1982 The middle atlantic bight cold pool: evolution of the temperature structure during summer 1979. *J. Phys. Oceanogr.* **12**, 1019–1029.

KILLWORTH, P. D 1983*a* Long-wave instability of an isolated front. *Geophys. Astrophys. Fluid Dyn.* **25**, 235–258.

KILLWORTH, P. D 1983*b* On the motion of isolated lenses on a beta plane. *J. Phys. Oceanogr.* **13**, 146–167.

KNESSL, C. & KELLER, J. B. 1995 Stability of linear shear flows in shallow water. *J. Fluid Mech.* **303**, 203–214.

LE SOMMER, J., SCHERER, E. & ZEITLIN, V. 2006 Inertial motions during the transient adjustment of a density anomaly in the equatorial ocean: application to the western Pacific warm pool. *J. Phys. Oceanogr.* **36**, 2270–2282.

PALDOR, N. & GHIL, M. 1990 Finite-wavelength instabilities of a coupled density front. *J. Phys. Oceanogr.* **20**, 114–123.

Poulin, F. J. & Flierl, G. R. 2003 The nonlinear evolution of barotropically unstable jets. *J. Phys. Oceanogr.* **33**, 2173–2192.

Reznik, G. M., Zeitlin, V. & Ben Jelloul, M. 2001 Nonlinear theory of geostrophic adjustment. Part 1. Rotating shallow water model. *J. Fluid Mech.* **445**, 93–120.

Ripa, P. 1983 General stability conditions for zonal flows in a one-layer model on the β plane or the sphere. *J. Fluid Mech.* **126**, 463–489.

Ripa, P. 1987 On the stability of elliptical vortex solutions of the shallow-water equations. *J. Fluid Mech.* **183**, 343–363.

Rubino, A., Dotsenko, S. & Brandt, P. 2003 Near-inertial oscillations of geophysical surface frontal currents. *J. Phys. Oceanogr.* **33**, 1990–1999.

Sakai, S. 1989 Rossby–Kelvin instablility: a new type of ageostrophic instability caused by a resonance between Rossby waves and gravity waves. *J. Fluid Mech.* **202**, 149–176.

Smith, P. C. 1976 Baroclinic instability in the Denmark strait overflow. *J. Phys. Oceanogr.* **6**, 355–371.

Trefethen, L. N. 2000 *Spectral Methods in Matlab*. SIAM.

Vanneste, J. 1998 A nonlinear critical layer generated by the interaction of free Rossby waves. *J. Fluid Mech.* **371**, 319–344.

Zeitlin, V. 2007 Nonlinear wave phenomena in rotating shallow water with applications to geostrophic adjustment. In *Nonlinear Dynamics of Rotating Shallow Water: Methods and Advances* (ed. V. Zeitlin), Elsevier, pp. 257–321.